CrossMark
click for updates

Comparison of the solar photocatalytic activity of ZnO–Fe$_2$O$_3$ and ZnO–Fe^0 on 2,4-D degradation in a CPC reactor†

M. L. Maya-Treviño, M. Villanueva-Rodríguez, J. L. Guzmán-Mar, L. Hinojosa-Reyes and A. Hernández-Ramírez*

In this work a comparative study of the catalytic activity of ZnO–Fe$_2$O$_3$ and ZnO–Fe^0 0.5 wt% materials was carried out in the degradation of 2,4-dichlorophenoxyacetic acid (2,4-D) as a commercial formulation Hierbamina®, using a compound parabolic collector (CPC) reactor. The catalysts were synthesized by the sol–gel method and characterized by X-ray diffraction, UV-Vis diffuse reflectance spectroscopy, Fourier transform infrared spectroscopy (FTIR) and scanning electron microscopy. The textural properties of solids were determined from N$_2$ adsorption isotherms using the Brunauer–Emmett–Teller (BET) method. The incorporation of Fe^0 onto ZnO was demonstrated by X-ray photoelectron spectroscopy analysis. The photocatalytic tests were performed at pH 7, using 10 mg L^{-1} of herbicide and 0.5 g L^{-1} of catalyst loading. The decay in herbicide concentration was followed by reversed-phase chromatography. A complete degradation of 2,4-D was achieved using ZnO–Fe^0 while 47% of herbicide removal was attained with ZnO–Fe$_2$O$_3$ mixed oxide for an accumulated energy $Q_{UV} \approx 2$ kJ L^{-1}. The removal percentage of total organic carbon (TOC) during the solar photocatalytic process was superior using ZnO–Fe^0, achieving 45% compared to the 15% obtained with the mixed oxide catalyst.

Introduction

The application of heterogeneous photocatalytic water purification processes has gained wide attention due to its effectiveness in degrading and mineralizing recalcitrant organic compounds as well as the possibility of using the solar UV and visible light spectrum.[1–3] The general understanding of the mechanism of photocatalysis is that photoabsorption of a semiconducting material (*e.g.* ZnO) occurs to excite electrons from the valence band (VB) to the conduction band (CB) leaving positive holes in the VB, *i.e.*, electron–hole pair (e^-–h^+) generation.[4] Oxidizing species (hydroxyl radicals, ˙OH, produced due to the photogenerated holes), which attack oxidizable contaminants, are generated producing a progressive break-up of molecules yielding low molecular weight organic compounds (*e.g.* carboxylic acids), inorganic ions, diluted inorganic acids, CO$_2$, and H$_2$O.[5]

ZnO, which can be obtained in a hexagonal wurtzite crystalline structure, is commonly used as a photocatalytic semiconductor.[6] It possess a wide band gap (3.2–3.37 eV)[6,7] and is one of the most important functional oxides, because of its direct band gap, large excitation binding energy,[8] and good carrier mobility.[9]

Despite the positive attributes of this semiconductor material, there are some drawbacks associated with its use: charge carrier recombination occurs very fast and the large band gap does not allow the utilization of visible light. Therefore, it is of great interest to separate the electron–hole pairs effectively to increase the photon efficiency and extend the absorption wavelength into the visible light region.[10] The modification of ZnO with metal oxides (*e.g.* Fe$_2$O$_3$) or transition metals (*e.g.* Fe, Ni, Mn, Co and Cu) allow enhancing these characteristics.[6,11–13]

The use of solar irradiation to power this process is environmentally attractive, and has a potential to reduce the cost of this technology. In addition to small scale studies, several pilot plant experiments have been performed in order to test the applicability of solar photocatalysis for wastewater treatment. One of the best options of reactors for photocatalytic applications using sunlight is the compound parabolic collector (CPC) reactors. The advantages of CPC reactors are: the possibility of using solar UV radiation coming from all directions in

Universidad Autónoma de Nuevo León, UANL, Facultad de Ciencias Químicas, Cd. Universitaria, San Nicolás de los Garza, Nuevo León, C.P. 66451, México. E-mail: aracely.hernandezrm@uanl.edu.mx

This journal is © The Royal Society of Chemistry and Owner Societies 2015

Photochem. Photobiol. Sci., 2015, **14**, 543–549 | 543

the sky (global UV radiation), simplicity of construction and operation, turbulent flow regime (which improves mass transfer), and high reduction of the vaporization of volatile pollutants.[14]

Therefore, in this work, $ZnO–Fe_2O_3$ and $ZnO–Fe^0$ were synthesized by the sol–gel process and their photocatalytic activity under solar light was evaluated in a CPC reactor on the degradation of 2,4-dichlorophenoxyacetic acid (2,4-D), one of the most widely used agrochemicals, which has provided control of broadleaf weeds in both agricultural fields and non-cropland grasses.[15,16]

Experimental

Reagents

Zinc acetate dihydrate ($Zn(CH_3COO)_2·2H_2O$) and iron(III) acetylacetonate ($Fe(C_5H_7O_2)_3$) used for the synthesis of the catalyst were supplied by Sigma-Aldrich. Commercial nano Fe^0 was supplied from Alfa Aesar. Ammonium hydroxide was provided by J.T. Baker. A commercial herbicide Hierbamina® (2,4-D) was used as received. The 2,4-D analytical standard (PESTANAL®) purchased from Sigma-Aldrich was used for chromatographic analyses.

Photocatalyst synthesis

Both semiconductor materials were synthesized by the sol–gel method. Mixed oxide synthesis (0.5 wt% of Fe_2O_3) was carried out as described in a previous study.[11] $ZnO–Fe^0$ was synthesized at pH 8.5, concentrated NH_4OH was added to zinc acetate solution (0.06 moles per 250 mL of water), and 0.5 wt% commercial nano Fe^0 (10–30 nm) was incorporated. The reaction mixture was maintained at room temperature until a gel was formed; once the colloid was observed, it was aged, dried in a water bath at 75 °C (fresh sample) and then calcined for 4 h in an electrical furnace at 450 °C under a N_2 inert atmosphere.

Characterization

The powder XRD patterns of the samples were recorded on a Siemens D-5000 diffractometer using Cu Kα radiation (λ = 1.5418 Å) at a scanning rate of 0.05° min^{-1} for 2θ ranging from 10 to 85°.

From the XRD pattern, the Scherrer formula was used to estimate the average crystallite size of the synthesized particles:

$$D = \frac{k\lambda}{\beta \cos \theta} \qquad (1)$$

where D is the crystallite size, λ is the X-ray wavelength, β is the half-height width of the diffraction peak of wurtzite (101), and the scale factor k = 0.89 depends on the shape of the grains, which is always close to unity.[17–19]

A UV-Vis spectrophotometer (Thermo Scientific Nicolet, model: Evolution 300 PC) with an integrating sphere (TFS-Praying Mantis) was used for diffuse reflectance measurements to establish the optical band gap. A $BaSO_4$ sample (Spectralon) was analyzed as a reference.

The materials were mixed with KBr and pressed under 7 tons cm^{-2} to obtain transparent pellets which were then analyzed using a Perkin Elmer FT-IR Spectrometer Paragon 1000 PC in the range from 450 to 4500 cm^{-1}.

The nitrogen adsorption isotherms of the samples were measured using an Autosorb-1 instrument (Quantachrome Corporation), and the surface area was calculated by the BET equation.

The surface morphology of the catalyst was studied using a scanning electron microscope (JEOL model JSM-6510LV).

X-ray photoelectron spectroscopy (XPS) was recorded with a Riber LDM 32, Scanning Auger Microscope PHI-595. The shift of binding energy due to relative surface charging was corrected using the C 1s level at 284.6 eV as an internal standard.

For total iron content in the $ZnO–Fe^0$, the catalyst sample (0.06 g) was digested in a block digester with a mixture of concentrated HF, HNO_3 and HCl (1 : 3 : 1) at 95 °C for 3 h. Then, the dissolved sample was analyzed by atomic absorption spectroscopy (AAS), using a Varian 220FS, SpectrAA model with an iron hollow cathode lamp photron at 248.3 nm (current intensity: 5 mA).

Photocatalytic tests

Photocatalytic experiments were carried out in a CPC reactor using 10 mg L^{-1} of 2,4-D at neutral pH, and 0.5 g L^{-1} of catalyst loading. The solar CPC photoreactor consisted of five borosilicate glass tubes and was used as only one tube to test the photocatalytic process; each tube connects two anodized aluminum parabolic reflectors. The reactor was operated in a recirculation mode using a 13 L recycle feed tank and a recycling centrifugal pump that delivered 21 L min^{-1}. The system was irradiated with solar light between October and December, 2013, in Monterrey, Mexico (latitude: 27°49′ north, longitude: 100°18′ W).

Solar ultraviolet radiation (UV) was measured by a global UV radiometer (Delta Ohm HD 2102.2) and it was collected every 10 min. Thus, the average incident radiation on the reactor surface ($\overline{UV}_{G,n}$) was calculated.

A mathematical approach was used for the treatment of the data obtained in solar experiments taking into account the relationship between experimental time (t), plant volume (V_t), collector surface (A_r) and the radiant power density ($U_{VG} = W_{UV}m^{-2}$) measured by a specific UV radiometer. Consequently, the amount of energy collected by the reactor (per unit of volume) from the beginning of the treatment until each sample is collected is found by:

$$Q_{UV,n} = Q_{UV,n-1} + \Delta t_n \overline{UV}_{G,n} \frac{A_r}{V_t};$$
$$\Delta t_n = t_n - t_{n-1} \qquad (2)$$

where t_n is the experimental time of each sample and $Q_{UV,n}$ is the accumulated energy (per unit of volume, kJ L^{-1}) incident on the reactor for each sample taken during the experiment.[20]

The progress of the reaction was followed taking aliquots every 30 min. The samples were filtered through a 0.20 µm Nylon syringe filter. Then, the herbicide concentration decay was monitored by reversed-phase chromatography (Perkin Elmer, series 200) using a C18 Phenomenex column (5 µm, 150 × 3 mm) and a UV detector (λ = 229 nm). The mobile phase was acetonitrile: 0.2% (v/v) acetic acid, pH 3.5 (40 : 60) at a 1 mL min^{-1} flow rate. Mineralization was followed by measuring the abatement of total organic carbon (TOC) with a Shimadzu-TOC V$_{CSH}$ analyzer.

Results

Characterization

An exhaustive characterization of the mixed oxide ZnO–Fe$_2$O$_3$ was reported on previously published work.[11] The wurtzite crystalline phase (JCPDS 36-1451) was identified from the XRD diffraction patterns in both modified semiconductors (data not shown). However, the reflections related to Fe^0 or Fe$_2$O$_3$, respectively, were not detected. The total iron content in the material was analyzed by atomic absorption spectroscopy indicated 0.47% content of Fe, which was in agreement with the expected value of Fe in the ZnO network (0.50%).

The incorporation of Fe^0 in the ZnO matrix was proved by the comparison of the XRD diffraction pattern of this catalyst with that of the prepared sol–gel ZnO in the range from 30 to 40 2θ. As can be seen in Fig. 1, the strongest signals of the wurtzite phase were observed, where the peaks of modified ZnO–Fe catalyst shifts towards higher values of 2θ.

It is well known that iron exists in both stable valence states, Fe^{2+} and Fe^{3+}. If Fe is present in the structure as Fe^{2+}, the reflection peaks shift towards the lower angle due to its bigger ionic radii (0.78 Å) than Zn^{2+} (0.74 Å). Otherwise, if it exists in the Fe^{3+} state (0.68 Å) then the peak shift should take place towards the higher 2θ angle.[21,22] It means that the Fe^{3+} ions occupy the regular lattice site of Zn^{2+} ions. This ion substitution produces crystal defects and charge imbalance in the
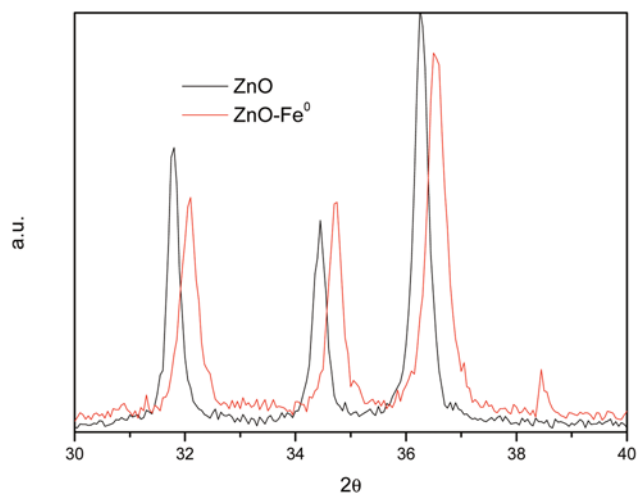

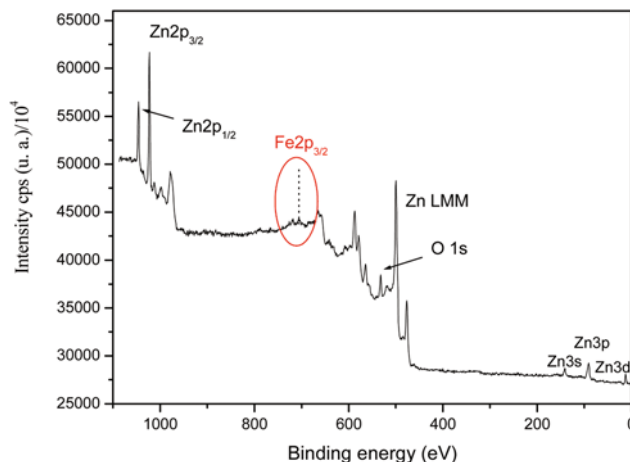**Fig. 1** Diffraction patterns of sol–gel ZnO and ZnO–Fe^0 catalysts.

Fig. 2 XPS spectrum of ZnO–Fe^0.

ZnO structure.[23] This shifting along with the decrease in signal intensity of the main characteristic peaks indicates the incorporation of Fe as Fe^{3+} in the ZnO matrix.[23,24]

Fig. 2 shows the XPS spectrum of the ZnO–Fe^0. The O 1s peak was observed at approximately 531 eV, and Zn 2p$_{3/2}$, Zn 2p$_{1/2}$ at 1022 and 1045 eV, respectively. The low binding energy peak of the O 1s spectrum can be attributed to the O$_2^-$ ions on the wurtzite structure of the hexagonal Zn^{2+} ion array, which are surrounded by zinc atoms with the full supplement of nearest-neighbor O$_2^-$ ions.[25,26] Both peaks corresponding to Zn 2p (Zn 2p$_{3/2}$ and Zn 2p$_{1/2}$) could be attributed to the binding energy of Zn–O, which confirms that Zn exists only in the oxidized state.[26–28] The spectrum showed peaks in the range between 20 and 200 eV as well as Zn 3d, Zn 3p, and Zn 3s peaks. The low intensity peak at 707 eV suggests the presence of the elemental metallic iron corresponding to the 2p$_{3/2}$ of Fe^0 and the peak at 711 eV corresponds to the 2p$_{3/2}$ of Fe^{3+}.[27,29,30]

According to the results from the XRD pattern and the XPS spectrum, Fe^{3+} (as iron oxide) and Fe^0 are present in the ZnO matrix, which could cause a synergistic effect to enhance the activity in the photocatalytic process. This effect could be explained as follows: when the ZnO–Fe^0 catalyst is illuminated an electron from the valence band (VB) is transferred to the conduction band (CB) generating an electron–hole pair. Therefore, due to the Schottky barrier effect, the electron flows into Fe^0 from the CB of ZnO and the hole of Fe^0/iron oxide flows back to the VB of ZnO, which could retard the electron–hole recombination improving the photocatalytic process.[31]

The surface morphology of the catalysts was studied by SEM analysis. As can be seen in Fig. 3, nanosized crystals tend to agglomerates resulting in the formation of particles of less than 100 nm. Those agglomerates are characteristics of the materials synthesized by the sol–gel method.

The band gap of ZnO–Fe^0 was calculated by the Kubelka–Munk function based on the following equation:
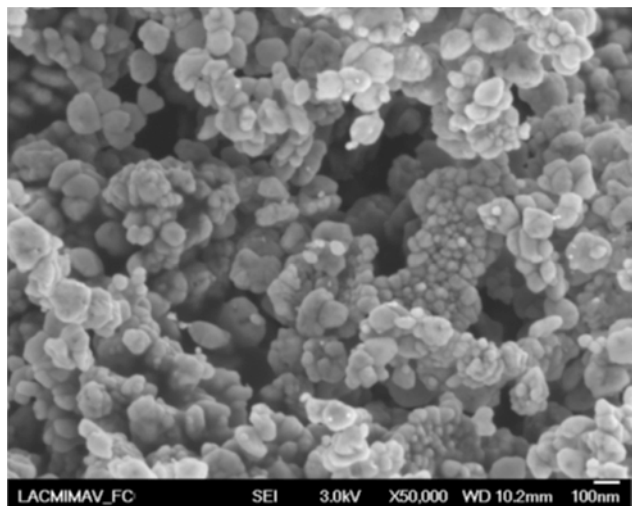
$$F(R) = \frac{(1-R)^2}{2R} \tag{3}$$

This journal is © The Royal Society of Chemistry and Owner Societies 2015

Photochem. Photobiol. Sci., 2015, **14**, 543–549 | 545

Fig. 3 SEM image of ZnO−Fe^0.

Table 1 E_g values, specific surface area and crystallite size of the photocatalytic semiconductors

Catalyst	E_g (eV)	Specific surface area ($m^2 g^{-1}$)	Crystallite size (nm)
ZnO–Fe^0	2.8	20.9	22.6
ZnO–Fe$_2$O$_3$	3.0	12.8	23.8
ZnO	3.2	18.5	26.1

where R is the reflectance, and $F(R)$ is proportional to the extinction coefficient (α). The basic Kubelka–Munk model assumes the diffuse illumination of the particulate coating. A modified Kubelka–Munk function can be obtained by multiplying the $F(R)$ function by $h\nu$ using the corresponding coefficient (n) associated with an electronic transition as follows: $(F(R)*h\nu)^n$.[32] For ZnO, $n = 1/2$ because a direct allowed transition is presented.

Fig. 4 depicts the plots of $(F(R)*h\nu)^{1/2}$ *vs.* $h\nu$ for the synthesized photocatalysts and sol–gel ZnO. An intense adsorption edge at approximately 3.0–3.2 eV, which corresponds to a charge transfer process from the valence band to the conduction band of the semiconductor oxide was observed.[33] This signal was assigned to the absorption edge of the zinc oxide, which presents a displacement towards lower energy values in ZnO–Fe^0 and ZnO–Fe$_2$O$_3$, thus narrowing the band gap compared with the theoretical value reported in the literature
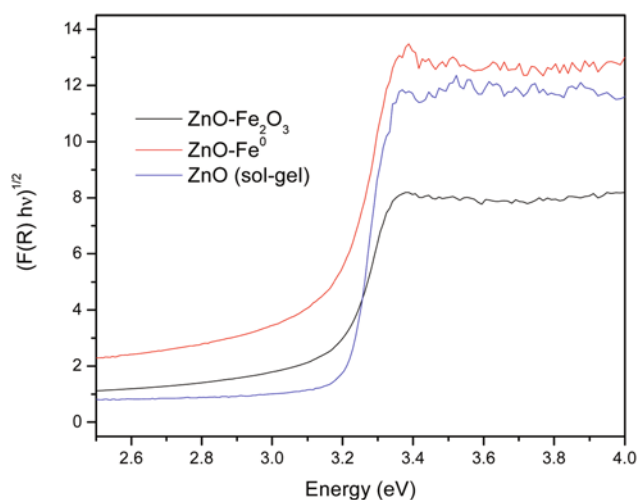
(3.2–3.3 eV).[6,7] This displacement was attributed to the small amount of iron (0.5 wt%) in both zinc oxide materials.

The E_g value, specific surface area and crystallite size of these catalysts are reported in Table 1. The catalyst ZnO–Fe^0 showed a higher E_g displacement towards lower energy values (2.8 eV) with respect to the mixed oxide (3.0 eV) and bare ZnO (3.2 eV). The higher shift in ZnO–Fe^0 is caused mainly by the presence of Fe^0 and Fe^{3+} ions in the ZnO crystalline lattice and the nanosized synthesized material. Some authors have reported that the decrease of the band gap is mainly due to the sp–d spin exchange interaction between the band electrons and the localized d electrons of the transition-metal ion substituting the cation into ZnO lattice.[34,35] Hence, the ZnO–Fe^0 catalyst can be activated with lower energy taking advantage of the solar radiation.

The specific surface area of the ZnO–Fe^0 catalyst was higher (20.9 $m^2 g^{-1}$) with a decrease in the crystallite size (22.6 nm). The increase in the surface area favors the capacity to adsorb the pollutant and transfer the photogenerated charges increasing the heterogeneous photocatalytic process.[36,37]

The FT-IR spectra of both annealed catalysts (ZnO–Fe$_2$O$_3$ and ZnO–Fe^0) are presented in Fig. 5, where the absorption band observed at low energy frequencies is formed by the stretching vibration modes of Zn–O,[38] while the band at 3490 cm^{-1} is assigned to the stretching vibrations of hydroxyl groups chemically bonded to the oxide network; this signal was more intense in the ZnO–Fe^0 sample indicating higher degree of surface hydroxylation than in mixed oxide. It is well known that hydroxyl groups act as active sites or adsorption centers,[12,39] increasing the photocatalytic efficiency of the solid.
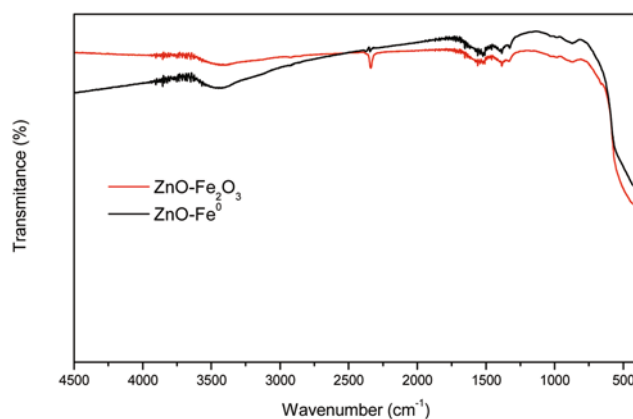

Fig. 4 Graphical representation of modified Kubelka−Munk: $(F(R)*h\nu)^{1/2}$ *vs.* energy for E_g calculation of ZnO, ZnO−Fe^0 and ZnO−Fe$_2$O$_3$ catalysts.

Fig. 5 FT-IR spectra of ZnO−Fe$_2$O$_3$ and ZnO−Fe^0 annealed at 450 °C.

546 | *Photochem. Photobiol. Sci.*, 2015, **14**, 543–549

This journal is © The Royal Society of Chemistry and Owner Societies 2015

Photocatalytic activity

The commercial herbicide formulation of Hierbamina® (479.5 g L^{-1} 2,4-dichlorophenoxyacetic acid, 2,4-D) was used for the evaluation of the photocatalytic activity of ZnO–Fe^0 and ZnO–Fe$_2$O$_3$ (0.5 wt%) in the solar CPC reactor.

The photocatalytic degradation and mineralization of the pollutant with both catalysts is shown in Fig. 6. For an accumulated energy $Q_{UV} \approx 2$ kJ L^{-1}, a complete degradation was achieved using the ZnO–Fe^0 while 47% degradation was reached using ZnO–Fe$_2$O$_3$. It is clear that incorporating Fe^0 into the zinc oxide structure improves the photocatalytic performance of the catalyst under solar light irradiation.

It is important to remark in the case of the ZnO–Fe^0 catalyst that the electronic activation of ZnO by solar light irradiation, provided the electrons to reduce Fe^{3+} back to Fe^{2+} (Fe^{3+} + e$^-$ → Fe^{2+} E_0 = 0.771 eV), and Fe^{2+} to Fe^0 (Fe^{2+} + 2e$^-$ → Fe^0 E_0 = −0.441 eV) which prevented the accumulation of the oxide layer on the Fe^0 surface, and this in turn maintains the iron content mostly as metallic iron.[31]

In general, most photocatalytic degradation reactions of organic compounds follow the Langmuir–Hinshelwood (L–H) model.[40]

$$r = -\frac{dC}{dt} = \frac{kKC}{1 + KC} \qquad (4)$$

where r represents the initial rate of photooxidation, C is the concentration of the reactant, t is the irradiation time, k is the rate constant of the reaction and K is the adsorption coefficient of the reactant.

Some authors described the influence of the photon flux (Ø) on both kinetic parameters (*i.e.*, k and K).[41] Despite this work, most researchers continue to use the L–H kinetic model for fitting the experimental results to a pseudo first order kinetic expression for the condition $kC \ll 1$ since it is adequate
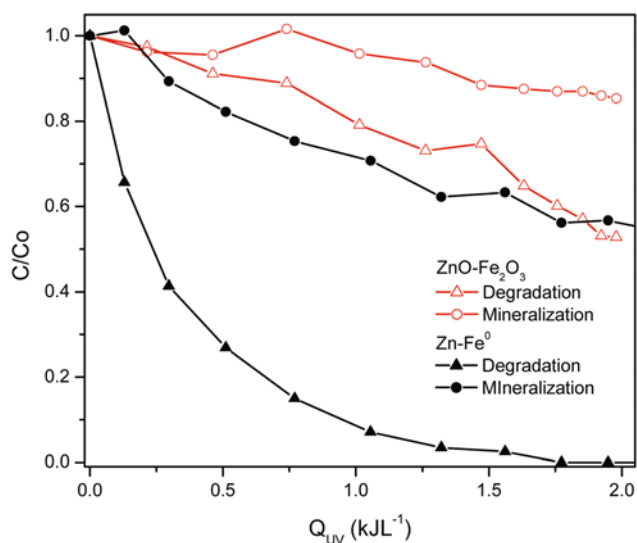
for a simplified characterization of this process in engineering applications. Therefore, the photocatalytic degradation rate of organic compounds at low concentrations is commonly described in terms of eqn (5):[40]

$$\ln \frac{Co}{C} = -k_{app}t \qquad (5)$$

where k_{app} is the apparent reaction rate constant which is not influenced by the photonic effect and t is the solar exposure time.[8]

The half-life ($t_{1/2}$) is the time required for the pesticide concentration to decrease to one-half the original value and is given by eqn (6):

$$t_{1/2} = \frac{\ln 2}{k_{app}} \qquad (6)$$

The degradation rate constant (k) was calculated from the slope obtained by a linear fit of ln (Co/C) as a function of time t. In Table 2 the degradation percentages as well as the kinetic parameters of 2,4-D degradation are shown.

Both semiconductor materials were active under solar light and induced the production of oxidizing reactive species, which attack the aromatic ring. However, the degradation using ZnO–Fe^0 material showed a higher rate constant and a shorter half-life time. Also the mineralization degree was higher using ZnO–Fe^0, where 45% was attained in comparison with 15% using ZnO–Fe$_2$O$_3$. Some research suggests that the hydroxyl radicals attack the aromatic ring, where its breakdown leads to the formation of 2,4-dichlorophenol, glycolic acid and subsequently chlorohydroquinone.[42] In a previous study, the photocatalytic activity of ZnO–Fe$_2$O$_3$ was evaluated in the degradation of 2,4-D commercial herbicide; the oxidation of the aromatic ring yields carboxylic acids such as oxalic, formic and acetic acids as well as chloride ions, identified as reaction byproducts.[11]

The low mineralization percentage of commercial 2,4-D with mixed oxide indicates that the aromatic ring breakdown was not efficiently conducted; however, with ZnO–Fe^0, the attack of hydroxyl radicals allowed to mineralize the molecule by almost 50%, where the residual TOC should correspond to intermediates such as hydroquinone and carboxylic acids.

According to the results, the ZnO–Fe^0 exhibited higher photocatalytic activity than the coupled oxide ZnO–Fe$_2$O$_3$, mainly due to its high surface area of 20.9 m^2 g^{-1} and low band gap energy of 2.8 eV, which increase the photocatalytic efficiency of ZnO–Fe^0.

Additionally, Fe$_2$O$_3$ and Fe^0 act as a trap for the photogenerated electrons on the ZnO preventing the electron–hole

Fig. 6 Evaluation of 2,4-D degradation in a CPC solar reactor using ZnO–Fe$_2$O$_3$ (△) degradation and (○) mineralization, using ZnO–Fe^0 (▲) degradation and (●) mineralization.

Table 2 Degradation percentage and kinetic parameters of 2,4-D oxidation using ZnO–Fe^0 and ZnO–Fe$_2$O$_3$

Catalyst	Degradation percentage	k (min^{-1})	$t_{1/2}$ (min)	R^2
ZnO–Fe^0	100	18.4 × 10^{-3}	38	0.9825
ZnO–Fe$_2$O$_3$	47	2.10 × 10^{-3}	330	0.9895

recombination; however, in the presence of oxygen, a reducing system as the Fe^0 can be converted into an oxidizing system, and the reductive power of iron can be used for oxidative reactions. Oxygen reacts with Fe^0 generating O_2^{2-}. The reduction of O_2 produces H_2O_2 as an intermediate and subsequent formation of hydroxyl radicals.[43] This mechanism produces a synergistic effect in the photocatalytic process, enhancing the catalyst activity for the degradation of 2,4-D.

Conclusions

ZnO–Fe^0 exhibited better photocatalytic activity than mixed oxide on the removal of the 2,4-D herbicide, achieving a complete degradation under solar radiation. The synergistic effect of Fe^{3+} formed in the ZnO–Fe^0 catalyst during the photocatalytic process using nanometric Fe^0, was explained in terms of the Schottky barrier effect, which retards the electron–hole recombination. This feature along with the higher surface area, the E_g displacement towards lower energy values and the hydroxylation degree of the annealed ZnO–Fe^0 catalyst, contributed to enhance its photocatalytic behavior with respect to the mixed oxide reaching higher percentage of pollutant mineralization which improves the efficiency of the degradation process.

Acknowledgements

Notes and references

1 R. R. Giri, H. Ozaki, T. Ishida, R. Takanami and S. Taniguchi, *Chemosphere*, 2007, **66**, 1610.

2 S. Ahmed, M. G. Rasul, W. N. Martens, R. Brown and M. A. Hashib, *Desalination*, 2010, **261**, 3.

3 S. Ahmed, M. G. Rasul, R. Brown and M. A. Hashib, *J. Environ. Manage.*, 2011, **92**, 311.

4 B. Ohtani, *J. Photochem. Photobiol., C*, 2010, **11**, 157.

5 S. Malato, P. Fernández-Ibáñez, M. I. Maldonado, J. Blanco and W. Gernjak, *Catal. Today*, 2009, **147**, 1.

6 M. M. Ba-Abbad, A. A. H. Kadhum, A. B. Mohamad, M. S. Takriff and K. Sopian, *Chemosphere*, 2013, **91**, 1604.

7 J. Rodríguez, R. J. Candal, J. Solís, W. Estrada and M. A. Blesa, *Solar Safe Water*, 2005, **9**, 135.

8 S. Navarro, J. Fenoll, N. Vela, E. Ruiz and G. Navarro, *J. Hazard. Mater.*, 2009, **172**, 1303.

9 M. Quintana, T. Edvinsson, A. Hagfeldt and G. Boschloo, *J. Phys. Chem. C*, 2007, **111**, 1035.

10 R. A. Mirzaie, F. Kamrani, A. A. Firooz and A. A. Khodadadi, *Mater. Chem. Phys.*, 2012, **133**, 311.

11 M. L. Maya-Treviño, J. L. Guzmán-Mar, L. Hinojosa-Reyes, N. A. Ramos-Delgado, M. I. Maldonado and A. Hernández-Ramírez, *Ceram. Int.*, 2014, **40**, 8701.

12 A. Hernández, L. Maya, E. Sánchez-Mora and E. Sánchez, *J. Sol-Gel Sci. Technol.*, 2007, **42**, 71.

13 B. M. Rajbongshi and S. K. Samdarshi, *Appl. Catal., B*, 2014, **144**, 435.

14 E. R. Bandala, C. A. Arancibia-Bulnes, S. L. Orozco and C. A. Estrada, *Sol. Energy*, 2004, **77**, 503.

15 S. P. Kamble, S. P. Deosarkar, S. B. Sawant, J. A. Moulijn and V. G. Pangarkar, *Ind. Eng. Chem. Res.*, 2004, **43**, 8178.

16 L. Wojnárovits and E. Takács, *Radiat. Phys. Chem.*, 2014, **96**, 120.

17 R. E. Dinnebier and S. J. L. Billinge, in *Principles of powder diffraction*, ed. R. E. Dinnebier and S. J. L. Billinge, RCS Publishing, Cambridge, UK, 2008, pp. 1–19.

18 K. Lv, J. Li, X. Qing, W. Li and Q. Chen, *J. Hazard. Mater.*, 2011, **189**, 329.

19 N. A. Ramos-Delgado, L. Hinojosa-Reyes, J. L. Guzman-Mar, M. A. Gracia-Pinilla and A. Hernández-Ramírez, *Catal. Today*, 2013, **209**, 35.

20 S. Malato, J. Blanco, D. C. Alarcón, M. I. Maldonado, P. Fernández-Ibáñez and W. Gernjak, in *Photocatalytic detoxification of water with solar energy*, ed. D. Y. Goswami, Earthscan, London, 2007, 17, 130.

21 P. Dhiman, J. Chand, A. Kumar, R. K. Kotnala, K. M. Batoo and M. Singh, *J. Alloys Compd.*, 2013, **578**, 235.

22 T. Pandiyarajan, R. Udayabhaskar and B. Karthikeyan, *Spectrochim. Acta, Part A*, 2013, **103**, 17.

23 M. M. Hassan, W. Khan, A. Azama and A. H. Naqvi, *J. Lumin.*, 2014, **145**, 160.

24 P. Dhiman, K. M. Batoo, R. K. Kotnala, J. Chand and M. Singh, *Appl. Surf. Sci.*, 2013, **287**, 287.

25 X. Q. Wei, B. Y. Man, M. Liu, C. S. Xue, H. Z. Zhuang and C. Yang, *Physica B*, 2007, **388**, 145.

26 S. Aksoy, Y. Caglar, S. Ilican and M. Caglar, *J. Alloys Compd.*, 2012, **512**, 171.

27 C. D. Wanger, W. M. Riggs, L. E. Davis, J. F. Moulder and G. E. Muilenberg, *Handbook of X-ray Photoelectron Spectroscopy*, Perkin Elmer Corporation, Minnesota, USA, 1979.

28 Y. Caglar, *J. Alloys Compd.*, 2013, **560**, 181.

29 X. Li, D. W. Elliott and W. Zhang, *Crit. Rev. Solid State Mater. Sci.*, 2006, **31**, 111.

30 Y. P. Sun, X. Q. Li, W. X. Zhang and H. P. Wang, *Colloids Surf., A*, 2007, **308**, 60.

31 W. P. Hsieh, J. R. Pan, C. Huang, Y. C. Su and Y. J. Juang, *Sci. Total Environ.*, 2010, **408**, 672–679.

32 R. López and R. Gómez, *J. Sol-Gel Sci. Technol.*, 2012, **61**, 1.

33 S. Sakthivel, S. U. Geissen, D. W. Bahnemanna, V. Murugesan and A. Vogelpohl, *J. Photochem. Photobiol., A*, 2002, **148**, 283.

34 S. Kumar, R. Kumar and D. P. Singh, *Appl. Surf. Sci.*, 2009, **255**, 8014–8018.

35 C. Aydın, M. S. Abd El-sadek, K. Zheng, I. S. Yahia and F. Yakuphanoglu, *Opt. Laser Technol.*, 2013, **48**, 447–45236.

36 M. Farbod and E. Jafarpoor, *Mater. Lett.*, 2012, **85**, 47–49.

37 A. Di Paola, E. García-López, G. Marcì and L. Palmisano, *J. Hazard. Mater.*, 2012, **211–212**, 3–29.

548 | *Photochem. Photobiol. Sci.*, 2015, **14**, 543–549

This journal is © The Royal Society of Chemistry and Owner Societies 2015

38 J. Ferraro, *Low frequency vibrations of inorganic and coordination compounds*, Plenum Press, New York, 1971, 72–74.

39 Z. Ding, GQ. Lu and PF. Greenfield, *J. Phys. Chem. B*, 2000, **104**, 4815.

40 J. Fenoll, P. Flores, P. Hellín, C. M. Martínez and S. Navarro, *Chem. Eng. J.*, 2012, **204–206**, 54.

41 S. Brosillon, L. Lhomme, C. Vallet, A. Bouzaza and D. Wolbert, *Appl. Catal., B*, 2008, **78**, 232.

42 C. Y. Kwan and W. Chu, *Water Res.*, 2004, **38**, 4213–4221.

43 A. Correia de Velosa and R. F. Pupo Nogueira, *J. Environ. Manage.*, 2013, **121**, 72.